ELSEVIER

Contents lists available at ScienceDirect

Geothermics

journal homepage: www.elsevier.com/locate/geothermics



Geothermal field development optimization under geomechanical constraints and geological uncertainty: Application to a reservoir with stacked formations

S.P. Szklarz^a, E.G.D. Barros^{a,*}, N. Khoshnevis Gargar^a, S.H.J. Peeters^a, J.D. van Wees^{a,b}, V. van Pul-Verboom^a

ARTICLE INFO

Keywords: Field development planning Optimization under uncertainty Stacked reservoirs Constrained optimization Fault stability constraints

ABSTRACT

In this work, numerical optimization based on stochastic gradient methods is used to assist geothermal operators in finding improved field development strategies that are robust to accounted geological uncertainties. Well types, production rate targets and well locations are optimized to maximize the economics of low-enthalpy heat recovery in a real-life case with stacked reservoir formations. Significant improvements are obtained with respect to the strategy designed by engineers. Imposing fault stability constraints impacts significantly the optimal configurations, with coordinated well rates and placement playing a key role to boost efficiency of geothermal production while keeping stress change effects to acceptable limits.

1. Introduction

Low-enthalpy geothermal energy has gained attention worldwide due to its potential to contribute to sustainable and clean energy solutions (Fridleifsson et al., 2008; Younger, 2015; Anderson and Rezaie, 2019; Soltani et al., 2019; De Giorgio et al., 2020). Low-enthalpy geothermal energy plays a crucial role in achieving the goals set by the Paris Agreement, as it offers a renewable and low-carbon alternative to traditional energy sources (Seo, 2017). By reducing reliance on fossil fuels and decreasing carbon emissions associated with heating, these systems contribute to the global effort to limit temperature rise and combat climate change.

Countries around the world are increasingly recognizing the potential of low-enthalpy geothermal energy and incorporating it into their energy portfolios (Birkle and Bundschuh, 2007; Andritsos et al., 2011; Arola et al., 2014; Dhansay et al., 2014; Rubio-Maya et al., 2015). Governments, businesses, and communities are encouraging the adoption of these technologies to not only meet climate targets but also to achieve energy security and promote sustainable development (Martín-Gamboa et al., 2015; Amoatey et al., 2021). In line with the global trend towards sustainable energy, the Dutch government aims at phasing out the use of fossil energy sources and transitioning to a

carbon-neutral energy system by 2050. To meet the targets of the global climate agreement, the heating sector must attain a decline of 20 megatons (Mt) CO₂-equivalent emissions by 2030, followed by an additional reduction of 36 Mt by 2050 (Schoof et al., 2018). With a high potential for large-scale sustainable heat generation, geothermal energy emerges as a promising solution.

In this context, increasing the cost-effectiveness of recovering heat from subsurface reservoirs can play a crucial role in advancing the successful execution of the energy transition strategy. The efficiency of heat production from geothermal wells and the associated economics of geothermal projects can be maximized through model-based optimization to determine improved field development strategies to exploit the geothermal resources. The abovementioned upscaling of geothermal activities can considerably benefit from the incremental value to be unlocked by the adoption of optimized development concepts and the respective learnings derived from optimization for the specificities of geothermal reservoirs. The suboptimal character of the current practices in geothermal development planning has been highlighted in recent studies. Process-based models and surrogate models (Akin et al., 2010; Kim et al., 2010; Yapparova et al., 2014; Chen et al., 2015; Wachowicz-Pyzik et al., 2020; Blank et al., 2021) have been used to optimize the well placement in geothermal systems. Most of these models are

E-mail address: eduardo.barros@tno.nl (E.G.D. Barros).

^a TNO, Applied Geosciences, Energy Transition, the Netherlands

^b Geosciences, Utrecht University, the Netherlands

^{*} Corresponding author.

based on simple box-model with one well doublet. Mijnlìeff and Van Wees (2009) and Willems et al. (2016) illustrated the need for improved well placement strategies using relatively simple engineering analysis. It was shown that, (Willems and Nick, 2019) while the potential for heat recovery is very high, the often applied 'first-come first served' approach based on doublet configurations only is expected to considerably decrease the total heat recovery potential. Kahrobaei et al. (2019) demonstrated the scope to optimize well placement strategies on a regional-scale, by showing that, with a predetermined number of vertical wells, optimized well locations can lead to substantial improvements in heat recovery.

In this study, we employ state-of-the-art model-based optimization techniques originally conceived in the context of oil and gas field development decisions and develop their application to the optimization of well type selection (producer or injector), production flow rates and well placement in geothermal reservoirs under geological uncertainty. The optimization framework used relies on modern stochastic gradient-based methods to enable robust optimization over an ensemble of model realizations in a computationally efficient manner (Fonseca et al., 2017). One of the key advantages of the stochastic gradient approach refers to the flexibility it confers to the workflow to be coupled with little effort to any type of model as a black-box. This allows the optimization framework to be easily employed in a variety of problems, ranging from the support of different types of field development decisions to assisting in the design of renewable energy systems (Barros et al., 2019, 2020a, 2020b, 2022; Hanea et al., 2019; Swamy et al., 2020).

We demonstrate the value of such a framework by applying it to a real-life geothermal reservoir in the Netherlands. The results obtained lead to useful insights from which the operators can potentially benefit to boost the efficiency of geothermal systems and to derive site-specific solutions with optimal development concepts tailored to the target geothermal reservoir which address robustness against the various uncertainties and ensure compliance to the constraints imposed. We note that, even though this study demonstrates the use of optimization as a means to assist practitioners in field development planning activities of a potential developing area, the results obtained, by no means, aim at providing guidelines or advice for any permit application. Throughout the study, practical limits regarding the stability of faults have been considered to showcase the capabilities of the optimization technology of imposing constraints within the optimization procedure and their impact on the optimized field development configurations. However, the obtained results with the assumed constraints are not meant to reflect a final general statement on the safety standards for geothermal operations.

This work aims at describing a modern and viable best-practice approach to improve geothermal field development planning in a broad sense for efficient exploitation of a large variety of geothermal resources. The ideas are presented in the form of the practical use of numerical optimization in a real-life complex case study in the Netherlands in order to provide a convincing demonstration of the value of optimization technology in a realistic context with societal relevance and specific challenges. Even though the obtained results are strongly oriented to specificities of the current Dutch geothermal landscape (i.e., low-enthalpy thermal energy production for direct heat use), the described approaches are generically applicable to other settings worldwide. By showcasing results of a real-life application, the intention is to ensure geothermal practitioners that numerical optimization can be applied in practice despite the complexity of the models (with uncertainties and constraints) and decisions involved. While the use of optimization is more disseminated in the oil and gas sector, there are very few academic sensitivity analysis studies in geothermal applications reported in the literature (e.g., Zaal et al. 2021). Therefore, to the best of our knowledge, this is first paper presenting the practical use of multi-disciplinary model-based optimization in a real-life geothermal field development case study.

This paper is structured as follows. In Section 2 we recap the

theoretical background on the framework for optimization under constraints and uncertainty. In Section 3 we outline the methodology followed to perform the work and achieve the goals of this study. Next, in Section 4, we describe the model of the real-life geothermal reservoir used in this study including the uncertainties accounted for, along with the optimization setup including the optimization variables considered and the implemented objective and constraint functions. Section 5 presents the results obtained from the optimization of field development. Finally, in Section 6 we conclude the paper and summarize the main findings.

2. Theoretical background

2.1. Computer-assisted optimization

Optimization is the process of seeking for the best possible solution of a particular problem. It involves identifying relevant degrees of freedom that can be varied to produce an effect on the performance of the system. In this work, the selected degrees of freedom or 'controls' to be optimized are the types of the wells to be drilled, their locations and the target rates assigned to the formations intercepted by the production wells. Optimization also implies the definition of the 'objective function' to be improved, here the discounted net present value to be maximized.

An optimization problem can be solved either manually using domain expertise of the practitioners assigned to find better solutions or through the use of computer-assisted optimization workflows. While manual optimization is often a process which is time-consuming and prone to errors, computer-assisted optimization leads to faster results which are less subject to human bias. However, the results from automated optimization workflows typically need to be analyzed and interpreted in order to be understood and accepted by practitioners and decision makers.

In field development optimization, we often deal with many complex design variables to be optimized in combination (e.g., trajectories of tens of wells, drilling order, time-varying well controls). Most optimization methods perform best when dealing with optimization variables that are continuous, and as few variables as possible. Many times, increased complexity implies a larger number of required variables. Therefore, the parametrization chosen (i.e., formulating the optimization problem with effective mathematical variables) is crucial. The parametrization choices followed in this study are discussed when introducing the optimization experiments in Section 5.

There are numerous methods for computer-assisted model-based optimization. These methods can be classified into two general classes, derivative-based and derivative-free techniques. Derivative- or gradient-based methods have been shown to be computationally more efficient than derivative-free methods. In particular, recent research efforts have led to the development of the Stochastic Simplex Approximate Gradient method (StoSAG) (Fonseca et al., 2017), which combines the efficiency of gradient-based approaches with the flexibility and ease of use of black-box derivative-free optimization. StoSAG has shown very good performance on a variety of optimization problems. In the following section we provide a brief description of this method.

2.1.1. Optimization under uncertainty

Disregarding uncertainty within model-based optimization workflows used to support design and planning activities may lead to unreliable conclusions, and therefore to poor decisions. Optimization procedure that includes uncertainty quantification throughout the iterations is usually referred to as robust optimization. In order to take subsurface uncertainty into account when making field development and operational decisions, there is a need to work with multiple geological model realizations (i.e., an ensemble of models). Each model realization is characterized by a set of model parameters (or parameter vector **m**) describing the geological and flow properties of the reservoir (e.g., permeabilities, porosities, initial pressure and temperature

conditions). By constructing a set of N_r geological model realizations $\mathbf{M} = \{ \mathbf{m}_1, \mathbf{m}_2, ..., \mathbf{m}_{Nr} \}$, a broad range of plausible reservoir behavior scenarios can be simulated to reflect the limited available knowledge of the subsurface. As a means to find a single optimal operational strategy that performs the best for all model realizations simultaneously and therefore most robustly against the uncertainties accounted for, one can optimize the average (over all models, typically assumed to be equiprobable) of the objective function, computed as:

$$\overline{J}(\mathbf{u}) = \frac{1}{N_r} \sum_{k=1}^{N_r} J^k(\mathbf{u}, \mathbf{m}_k), \tag{1}$$

where $\overline{J}(\mathbf{u})$ is the mean of the objective function value being optimized for a single strategy \mathbf{u} based on each $J^k(\mathbf{u},\mathbf{m}_k)$ which is the objective function evaluated for each k^{th} geological realization \mathbf{m}_k , and N_r is the number of geological realizations considered. The optimization method handles any objective function $J(\mathbf{u})$ the same way, therefore the mathematical notation adopted here is rather abstract. In Section 4.5.1, we will introduce the specific objective function considered in this optimization study.

As the number of model realizations increases for a more complete representation of complex uncertainties, the number of simulations required to perform the optimization tends to increase considerably. On this basis, the computational efficiency of the optimization method becomes important to render tractable optimization problems involving large-scale real-life models with time-consuming simulations. Particularly in this context, the StoSAG described next provides an attractive solution.

2.1.1.1. Stochastic gradient. The StoSAG method has shown to be powerful for optimization problems which need to consider uncertainty and need flexibility in terms of coupling with different simulators. To approximate the gradient of the objective function with respect to control variables (i.e., degrees of freedom subject to optimization). Around each solution, the algorithm varies all the control variables simultaneously by sampling of normally distributed deviations from the original control value to generate a set of perturbed control points. The objective function values for each of these new points are then evaluated (e.g., by performing the required techno-economic calculations). An approximate gradient is thereby computed through a linear regression of this set of perturbed controls and their respective objective function values. From this point on, a standard gradient descent optimizer can be employed in an iterative loop for the optimization - the calculated approximate gradient provides the direction to update the control variables in the next iteration. For robust optimization, when multiple model realizations are used to represent uncertainty, Fonseca et al. (2017) proposed the StoSAG formulation where each model realization is paired with a single control perturbation inspired by the approach followed by Chen et al. (2009), making the gradient estimation and optimization procedure computationally attractive in large-scale optimization problems with expensive simulation models. In this work we only leverage the StoSAG method in the optimization exercises to be presented next, therefore the description of method is not further detailed. For a more comprehensive explanation of the StoSAG method, we refer to Fonseca et al. (2017).

2.1.2. Constrained optimization

Solutions to real-life problems must often adhere to pre-defined restrictions. For instance, design configurations or operational strategies might only be accepted as valid or feasible if the characteristics of the system comply to the defined limits. These considerations also hold in the context of optimization, in which case the optimization procedure is expected to determine optimal solutions that honor all the imposed constraints. Generally, an optimization problem with non-linear constraints can be mathematically formulated as:

$$\label{eq:maxJ} \mbox{maxJ$}(\mbox{$u$}), \mbox{ subject to } \mbox{g}(\mbox{u}) \leq 0 \mbox{ and } \mbox{h}(\mbox{u}) = 0, \tag{2}$$

where $J(\mathbf{u})$ is the objective function value to be maximized, $\mathbf{g}(\mathbf{u})$ represents the set of inequality non-linear constraints and $\mathbf{h}(\mathbf{u})$ the set of equality constraints. Note that both the objective and the constraints are function of the same strategy \mathbf{u} being optimized, which means that there may be cases where there is a trade-off between maximizing the objective function against complying with the constraints.

In particular, seeking optimal solutions that are feasible in terms of non-linear constraints requires dedicated approaches, which belong in the realm of constrained optimization. A common approach to tackle constrained optimization problems is the Lagrangian approach, which consists of constructing the so-called Lagrangian function formed as:

$$\mathscr{L}(\mathbf{u}) = J(\mathbf{u}) + \boldsymbol{\mu}^{\mathrm{T}} \mathbf{g}(\mathbf{u}) + \boldsymbol{\lambda}^{\mathrm{T}} \mathbf{h}(\mathbf{u}), \tag{3}$$

where μ and λ are the sets of Lagrange multipliers. The Lagrangian function $\mathcal{L}(\mathbf{u})$ can then be used to derive a corresponding unconstrained optimization problem as a function of the original optimization variables and the Lagrange multipliers. In this context the solution of this kind of optimization problem with a gradient-based approach involves the calculation of the gradient of both the objective and constraint functions with respect to the control strategy \mathbf{u} , which can be computed using the StoSAG method. Like for the objective function, the optimization method handles any constraint functions $\mathbf{g}(\mathbf{u})$ and $\mathbf{h}(\mathbf{u})$ the same way, therefore the generic notation. In Section 4.5.3, we will introduce the specific constraint functions considered in this optimization study.

Constrained optimization via the Lagrangian approach can be achieved through different optimization algorithms. Our optimization framework used in this study currently supports two classes of algorithms, namely: (i) a quasi-Newton interior point based optimizer (OPT++ library by Meza et al. 2007) which employs a merit function penalizing constraint violations to guide the optimization, and (ii) a optimizer based on the method of feasible directions from the CONMIN library (Zoutendijk, 1960; Vanderplaats, 1984) which solves a sub-problem to find the descending feasible direction once constraint surfaces are reached during the optimization. Other methods for constrained optimization exist; for more information and some examples, we refer to (Zoutendijk, 1960; Vanderplaats, 1984; Meza et al., 2007).

For the case of robust optimization in this work, just like for the objective function when accounting for an ensemble of model realizations, the constraint functions are also computed and imposed as an average over the ensemble.

2.2. Optimization workflow

The EVEReST optimization framework (https://github.com/equinor/everest) used in this work leverages the strengths of the StoSAG method described above as a black-box gradient-based optimization approach to facilitate the setup of modular workflows and provide flexibility for users to tailor the framework to their specific applications. This allows users to focus on the use of domain knowledge to define the problem and interpret their model results, instead of spending effort on repetitive and time-consuming tasks such as manually setting up and running simulations to search for improved solutions. Once a first computational workflow with a series of required calculations is set, it is simple to adjust it to include additional optimization variables or to test different optimization approaches. Fig. 1 depicts schematically the steps taken in a typical optimization experiment with EVEReST.

The field development decisions are based on the subsurface models. Therefore, any workflow used to support decision making involves adjusting well-related boundary conditions in the subsurface simulation models. At each iteration, the control variables are translated into required inputs the reservoir flow simulator and the simulation runs for all the models are launched. Constraints and objectives can then be

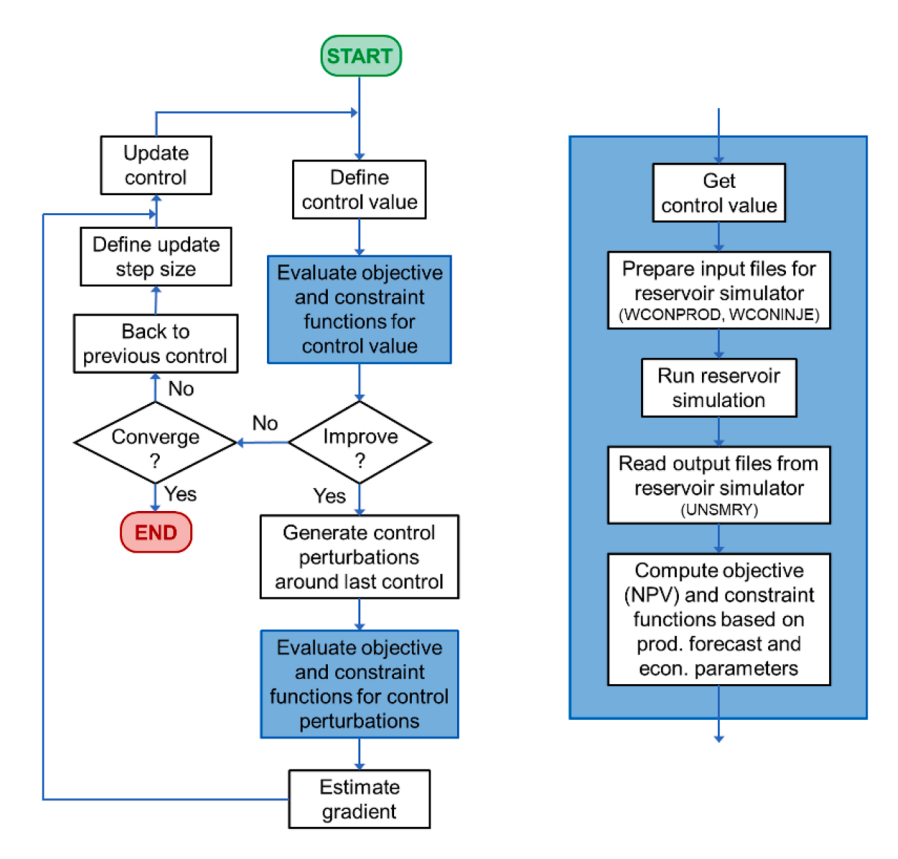


Fig. 1. Iterative optimization procedure followed by EVEReST (left) and steps of computational workflow tailored to the optimization of geothermal field development strategies (right).

computed from the simulation output and the direction to update the control variables (StoSAG gradient) is calculated. The calculation steps are repeated in the next iteration using the updated control variables, and the optimization continues through subsequent iterations until reaching convergence.

3. Methodology

The primary goal of this work is to deliver a recommended best field development strategy for our target real-life case study through the use of numerical optimization. A second goal is to gain understanding of the impact of adhering to imposed safety limits (i.e., fault stability) on the optimal field development strategy and expected techno-economic performance, by performing optimization with different settings (i.e., different optimization variables and constraint considerations). To achieve these goals, the work done consisted of the following steps:

- (1) Gather available information about local geology and field development base case (i.e., initial field development strategy provided by operator with well placement and well types defined based on engineering guess) of the area of interest
- (2) Construct an ensemble of model realizations of the real-life geothermal site to capture the underlying geological uncertainties
 - (a) Build geological model and account for uncertain static properties
 - (b) Prepare ensemble of dynamic models with realistic operational constraints
- (3) Formulate the optimization problem:
 - (a) Define economic assumptions to determine objective function
 - (b) Define fault stability calculation assumptions to determine constraint function

- (4) Perform optimization experiments for different optimization variables and with gradually increasing complexity:
 - (a) Unconstrained optimization (i.e., without fault stability considerations):
 - (i) Optimize well types (producers or injectors) for predefined well locations from the base case and fixed well production / injection rate targets
 - (ii) Optimize well production / injection rate targets for optimized well type configuration in (i)
 - (b) Constrained optimization (i.e., with stress-based fault stability considerations):
 - (i) Optimize well production / injection rate targets for optimized well type configuration
 - (ii) Optimize location of injectors starting from 4-well modification of optimized well type configuration
- (5) Analyze and compare results of optimization experiments performed in (4) to understand most influential variables, verify compliance to imposed constraints and derive case-specific insights

4. Case study

4.1. Geological setting

The area of interest is located in the Netherlands. The name and location of the formations and wells are anonymized in this study.

The target reservoirs for this study area are an Upper formation Member and a Lower formation Member (Van Adrichem Boogaert and Kouwe, 1993; Donselaar et al., 2015). The Lower formation Member consists mainly of channels, and fluvial plain deposits, where the sand is mostly concentrated in the channels and crevasse splays (Van Adrichem Boogaert and Kouwe, 1993; Donselaar et al., 2015). The Upper formation Member is separated from the Lower formation Member by a shale

interval that represents a sequence boundary, which was caused by a marine transgression (sea level rise) between the Lower and Upper formation Member (Den Hartog Jager, 1996). Like the Lower Member, the Upper formation Member also consists of fluvial deposits. The Upper formation Member was deposited during the late part of the Valanginian stage (Den Hartog Jager, 1996) and, like the Lower formation Member, the Upper formation Member also consists of fluvial deposits. These deposits consist of fine-to-coarse grained and gravelly sands which represent stacked distributary channel-systems deposited in a lower coastal-plain setting (Van Adrichem Boogaert and Kouwe, 1993). Given the fact that the Upper formation Member generally consists of coarser sand and less clay than the Lower formation Member, the depositional environment was likely more energetic (fluvial sediments deposited with higher velocities) than the one forming the Lower formation Member.

4.2. Geological models

The static geological model serves as input for the reservoir optimization modelling. It consists of 325,500 grid cells with an average increment of approximately 51 m in the horizontal J-direction, 43 m in the horizontal I-direction and 23 m in the vertical K-direction. Two target aquifer formations are located within the model separated by a clay interval (i.e., inactive layers in the reservoir simulation model).

The reservoir geometries and fault distributions of the static geological model were based on the interpretation of seismic data. Seismic-to-well ties were made for two existing wells in the area where check-shot was available. The well trajectories from existing wells in the area were obtained from the operators via the national data repository (NLOG, https://www.nlog.nl/). The regional velocity model VELMOD 3.1 was used to convert the time-based seismic horizons to depth (Pluymaekers et al., 2017). Based on seismic interpretation, two main faults were identified which are oriented roughly NW-SE (Figs. 2 and 3). The depth of both the Lower and Upper formation Member generally increases towards the west and southwest (Fig. 3). Note also that the thickness of the Lower formation Member increases towards the southwest (Fig. 3).

The created static models were populated with reservoir properties (i.e., fluvial facies, Net-to-Gross, porosity and permeability in the I, J and K directions) that were petrophysically derived from well-log, and well test data from existing nearby wells. The effective porosity logs were calculated by using the density, method and correcting for the shale volume in the rock (Alberty, 1992; Morton-Thompson and Woods, 1992). The permeability logs were derived by applying an established poro-perm relation valid for the reservoirs of interest in the case study region. Density logs and consequently porosity logs only existed for two wells within the case study region. Gamma-ray logs on the other hand were available for several more wells within the case study region.

Because a strong correlation exists between rock properties (e.g., porosity, permeability) and lithology, the gamma-ray logs were used to compute the rock's fluvial facies. This was done by applying a gamma-ray cut-off of 65 gAPI. An interval with a gamma-ray lower than 65 was classified as sandy channel deposits. An interval with a gamma-ray exceeding 65 gAPI was classified clay-rich floodplain deposits. Based on the gamma-ray cuts-off, net-to-gross logs were calculated, which were used to estimate the amount of sand in the Lower formation Member.

After the reservoir properties were calculated at the location of the existing wells, the properties were arithmetically upscaled. Based on the upscaled net-to-gross log, the model was stochastically populated with channel sands that followed the main paleo current direction from SE to NW. The Lower formation Member contains 79 % of channel sands with a mean width of 300 m (± 150 m). The Upper formation Member was modelled as one sandy package of 13.5 m thick. The remaining reservoir properties (i.e. porosity and permeability) were modelled away from the wells by applying Gaussian random function modelling and by taking into account a correlation with the presence of the fluvial facies (i.e. channel sand bodies vs. clay-rich floodplain deposits). A spherical variogram with a total sill of 1.0 and a nugget of 0.01 was considered. Overall, 50 model realizations were created for all the reservoir properties to model the reservoir properties away from the wells. The modelled porosity in the channel sands of the Upper formation Member varies between 14 and 19 %. The porosity in the channel sands of the Lower formation Member ranges between 12 and 21 %. The porosity for the clay-rich floodplain deposits was set at a constant 0.01. The horizontal permeability in the J direction that was used in the model ranges between 500 and 1500 mD for the channel sands in the Upper formation Member and between 50 and 300 mD for the channel sands in the Lower formation Member. The horizontal permeability for the clay-rich floodplain deposits was set at a constant 0. To account for vertical anisotropy, a value of $k_{h,J}/k_{v}=3.8$ was derived.

The model realizations include the uncertainties regarding transmissibility of the faults which refer to what extent the faults are able to transmit fluids. The uncertainties regarding fault transmissibility were addressed by calculating the shale gouge ratio (Yielding, 2002), which is based on the assumption that the composition of the fault gouge (i.e. the fractured material that forms the fault plane) follows directly from the bulk composition of the host rocks that has slipped as a particular point on the fault plane (Yielding, 2002).

4.3. Reservoir simulation models

Based on the static model, a dynamic model was built containing 325,000 grid cells from which 150,000 are active. The reservoir dimensions are approximately 4×4 km with $124\times 105\times 25$ grid cells in the x, y and z directions. The top and bottom formations, representing

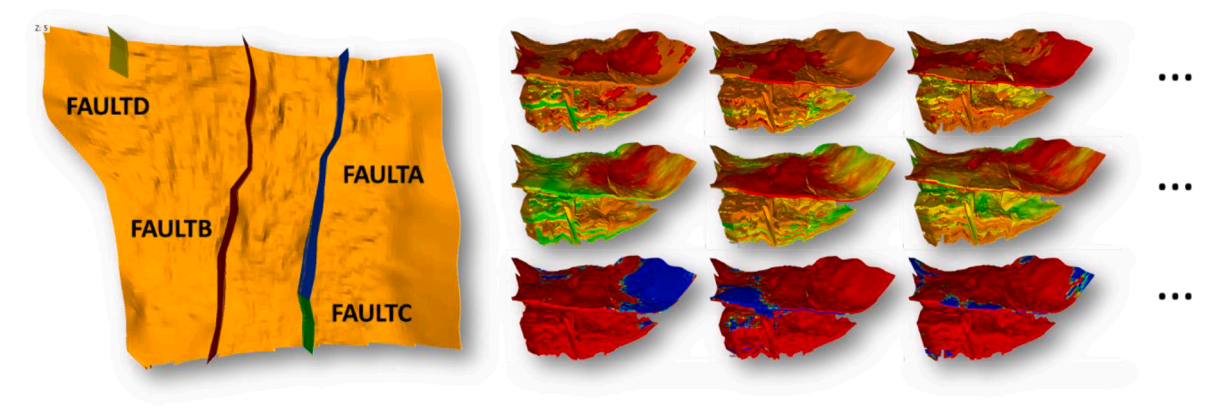


Fig. 2. The location of faults on the left (top view) and selected realizations with different geological properties on the right: permeability, porosity and net-to-gross.

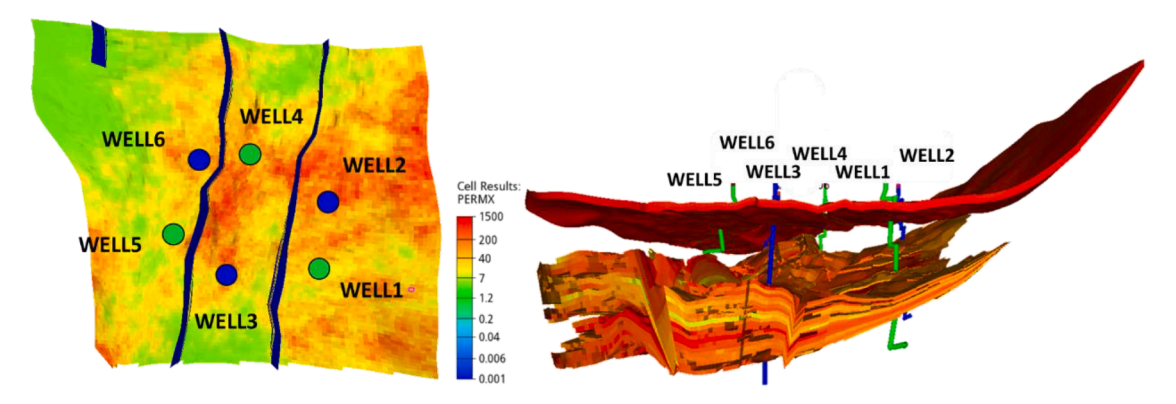


Fig. 3. One realization of the numerical model and the location of faults, planned wells (producers in green and injectors in blue) and top (Upper formation Member) and bottom (Lower formation Member) formations. Top view on the left and side view on the right.

Upper and Lower formations respectively, are separated by a vertical flow barrier. The Lower formation is significantly thicker than the Upper Sandstone. The faults split the reservoir formations into three lateral sections. There are three planned doublets in the model, including three deviated injection wells and three deviated producers (see Fig. 3). A preliminary well placement (with selected locations for the three producers and the three injectors) has been defined based on engineering guess by the operator to develop the geothermal site. This initial placement is the starting point for our optimization experiments.

Since no wells have been previously drilled in the area of interest, there is significant uncertainty on the geological characteristics of subsurface. This uncertainty is represented by $N_{\rm r}=40$ realizations of the numerical model with different flow properties such as permeability, porosity, net-to-gross and fault transmissibility. The faults have been initially defined as ranging from half-sealing to fully-open. However, due to clay smearing of the fault in the Lower formation, fault transmissibility multipliers have been reduced in Lower formation faults to a distribution with a lower mean and higher standard deviation. Note that this means that each model realization will have different fault transmissibility and each of the faults in the same model will have different transmissibility. Fig. 2 displays the model with the fault locations and some of the generated model realizations.

4.4. Model constraints

The dynamic simulation model was built within the open-source reservoir simulator OPM-Flow (Rasmussen et al., 2021). While constructing the model, three important modelling requirements and constraints were defined:

- Production targets from Upper and Lower formations should be controlled separately as additional degree of freedoms for the optimization exercise (e.g., assuming the availability of intelligent completions).
- Bottom-hole pressure (BHP) must comply with practical operational conditions (i.e., physically consistent pressure profile along the wellbore).
- Produced volumes must equal injected volumes in each of the two formations (i.e., complete voidage replacement in both formations by imposing full reinjection of produced volumes).

In order to control production rate targets to be assigned to the two formations, 12 simulation wells have been defined to represent the 6 wells in reality. Each well was split into two: a lower and an upper formation well. In order to ensure depth-consistent well pressure, the current BHP for each well in one of the formation was extracted to set the limits on the BHP for the corresponding well in the other formation. The minimum allowed difference in prescribed bottom-hole pressure

between the upper and lower well was imposed according to the difference in depth between the two formations of approximately 100 m (which corresponds to a hydrostatic difference in pressure of approximately 10 bar). In addition, realistic BHP limits were prescribed to the wells in the lower and upper formations individually. For the verification of consistent BHP behavior across the 40 model realizations, we refer to Fig. 4 which depicts the statistics of the difference in well BHP between bottom and top formation across all the 40 model realizations in the form of box-plots. Note that for all model realizations the difference in pressure is indeed never below 10 bar.

In order to ensure equal production and injection rates, the simulator uses the total production rate from each formation to set dynamically the target for total injection rate in the same formation. In addition, each well has its own maximum rate limit to prevent exceeding flow capacity.

4.5. Optimization setup

The objective function and the control variables are the key user-defined features of any optimization process. The control variables are changed by the optimizer to explore directions toward improved objective function values leading to the optimized solution.

In this paper, the well types (i.e., injector or producer) and well production rates are optimized to maximize the economics of the geothermal heat development project. For this purpose, the net present value (NPV) is a suitable objective function because it considers both project costs and revenues in a balanced way. Nevertheless, the optimization framework used in this project is suitable for any objective function and any types of controls.

4.5.1. Objective function

This study is aimed at maximizing the economics of heat production of the geothermal development over a production life-cycle of 30 years. A standard NPV formulation for doublet geothermal systems has been

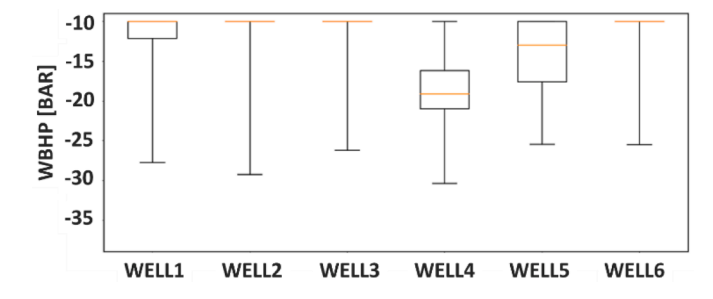


Fig. 4. Box-plots showing statistics of the differences in well BHP between bottom and top formation across 40 model realizations. The orange lines represent the averages, boxes represent the 25th and 75th quantiles and whiskers mark the maximum and minimum values.

used (van Wees et al., 2012, 2020; Vrijlandt et al., 2019). To account for the time-value of heat production and the associated costs, the discounted NPV is computed as

$$J_{\text{NPV}}(\mathbf{u}) = \sum_{k=1}^{N_t} \frac{\left(r_h \cdot e_{\text{prod},k}(\mathbf{u}) \cdot \Delta t_k - r_p \cdot \left(e_{\text{pump},k}^{\text{prod}}(\mathbf{u}) + e_{\text{pump},k}^{\text{inj}}(\mathbf{u})\right) \cdot \Delta t_k - c_k(\mathbf{u})\right)}{(1+b)^{t_k/\tau}},$$
(4)

where \mathbf{u} is the control vector, $e_{\mathrm{prod},k}$ is the heat production [J/s] during the k^{th} simulation time interval, $e_{\mathrm{pump},k}$ is the power consumed to operate the required pumps [J/s], Δt_k is the size of the k^{th} simulation time interval [s], c_k are the costs (CAPEX and OPEX), r_h is the heat price [ϵ /GJ] (including subsidy scheme guaranteeing a certain minimum price over a 15-year period), r_p is the electricity cost [ϵ /GJ] for the operations, b is the (yearly) discounting factor, t_k is the time at the k^{th} simulation time interval, τ is the reference time for discounting cashflow and N_t is the total number of simulation time intervals.

The produced power at each time interval $e_{\mathrm{prod},k}$ [J/s] is calculated as:

$$e_{prod,k} = q_k \rho_{\rm w} c_{\rm w} \Delta T_k, \tag{5}$$

where $q_k \, [\mathrm{m}^3/\mathrm{s}]$ is the volumetric production rate and $\Delta T_k \, [\mathrm{K}]$ is the difference between injection and production temperature at each simulation time-step k, $\rho_\mathrm{w} \, [\mathrm{kg/m}^3]$ is the water density and $c_\mathrm{w} \, [\mathrm{J/kg \cdot K}]$ is the water specific heat capacity.

The pumping costs are calculated for both injection and production wells, which is a function of the pumping power required, $e_{\text{pump},k}^{\text{prod.}}$ [J/s]. For producers, this depends on the efficiency of the pump (ε) , the production rates q_k [m³/s] and the pressure difference $\Delta P_{\text{prod},k}$ [bar] applied by the electrical submersible pumps (ESP) to lift the produced fluids to the surface facilities:

$$e_{\text{pump},k}^{\text{prod}} = \frac{q_k \Delta P_{\text{prod},k}}{\varepsilon}$$
 (6)

For the injectors, we assume that a booster pump is used at the surface (downstream of the heat exchanger) to inject the cold water into the wells. The power associated with the operation of the booster pump is calculated as:

$$e_{\text{pump},k}^{\text{inj}} = \frac{q_k \Delta P_{\text{inj},k}}{\varepsilon}.$$
 (7)

The CAPEX costs include all surface facility costs including heat exchanger, booster pumps, separators (if necessary), etc., which are assumed to be invested in the first year of project development. In this work, the costs for drilling are based on the drilled length of each well. ESPs have their own associated costs since they are replaced at regular intervals of the production wells. The OPEX costs for the producers and injectors are calculated individually. The values of the economic parameters used for the NPV calculation are indicated in Table 1.

Table 1 Economic parameters used in NPV.

Variable	value	unit
Pump efficiency, ε	65	%
Heat price, $r_{\rm h}$ (incl. subsidy)	5.0 for first 15 years	€/GJ
	2.5 for remaining 15 years	
Electricity cost, $r_{\rm p}$	13.3	€/GJ
Drilling cost	$2.0 imes 10^6$	€/km
Pump cost	1.0×10^6 (producers)	€/3 years
	0.5×10^6 (injectors)	€
CAPEX	$30 imes 10^6$	€
OPEX	1.95×10^{6}	€/year
Discount factor, b	9	%/year

4.5.2. Control variables

In field development optimization, we often deal with many complex design variables to be optimized in combination, e.g., trajectories of many wells, drilling order, time-varying well controls. In this work three types of decisions and therefore three types of control variables were considered in optimization:

- 1. Well types (producers or injectors): any configuration of 3 producers and 3 injectors
- 2. Well rate targets: allowed to vary in the [0, 350] m³/h range
- 3. Well locations: allowing the placement of vertical wells to vary across the entire extent of the reservoir

4.5.3. Constraints

In addition to the model constraints described in Section 4.4, there was also a need to define optimization constraints. We considered two types of constraints, i.e., the so-called input constraints and output constraints. The combined rates for Upper and Lower formations were limited by optimization input constraints to not exceed the maximum rate of $350 \, \text{m}^3/\text{h}$ for each well. Optimization output constraints were defined to limit the risk associated with the near-fault stress behavior caused by the development of the field, by considering stress change across the faults in different optimization experiments (Fig. 5).

In order to consider not only pressure but also the temperature effect on fault stability, the Coulomb stress change is calculated and considered as constraint in optimization experiments. Simulated pressure and temperature changes in the reservoir are used to calculate strain and stress changes at the fault locations. In case of spatially gradual and/or vertically layered, changes in temperature and pressure, the associated elastic strain and stress can be approximated with a model of uniaxial (vertical) strain and using the boundary condition that vertical total stress remains unchanged, in accordance with the weight of the overburden and horizontal strain is zero. The stress tensor can be used to calculate the Coulomb stress change or Shear Capacity Utilization (SCU) (Buijze et al., 2017). When the SCU is < 1 the failure strength of the fault element has not yet been reached and the element is responding elastically. Please note that the uniaxial approach for estimating stress changes and underlying parameters are tentative values and the primarily serve to showcase the capability to include fault stability considerations in the optimization procedure.

While pressure difference can be derived directly from the pressures calculated by the reservoir simulator, strain and stress changes are a function of both pressure and temperature changes determined by the flow simulator. In case of spatially gradual and/or vertically layered changes in temperature and pressure, the associated elastic strain and stress can be approximated with a model of uniaxial (vertical) strain and using the boundary condition that vertical total stress remains unchanged, in accordance with the weight of the overburden and the assumption of horizontal strain to be zero (Fjaer et al., 2008; Van Wees et al., 2014).

The effect of temperature and stress change (ΔT and ΔP) on vertical strain e_{zz} under uniaxial conditions is equal to (Fjaer et al., 2008) (Eqs. (1.123) and (12.10)):

$$e_{zz}(t) = \Delta T(t)\alpha_T \frac{(1+\nu)}{(1-\nu)} + \Delta P(t) \frac{(1-\nu-2\nu^2)}{(1-\nu)E},$$
 (8)

where $\Delta T(t)$ is the temperature change [K], α_T is the linear thermal expansion coefficient [1/K], ν is the Poisson's ratio, $\Delta P(t)$ is pressure change [Pa] and E is the Young's modulus [Pa]. Consequently, the changes in horizontal and vertical effective stress are given by Hooke's law, poro-elasticity and adopting Biot's constant equal to 1 (e.g., Fjaer et al. 2008, Zoback 2010):

$$\Delta \sigma'_{hH}(t) = e_{zz} (t) \frac{E}{(1+\nu)} - \Delta P(t)$$
 (9)

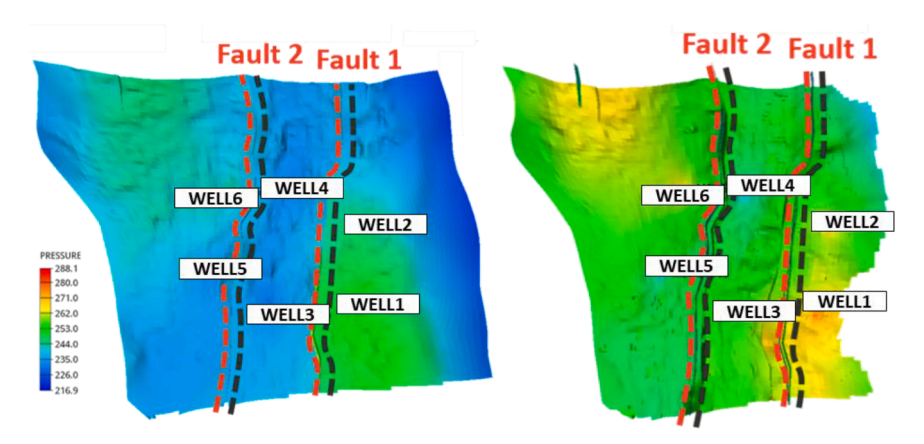


Fig. 5. Marked cross sections of the grid on both sides of each fault. Upper formation layer on the left and Lower formation layer on the right. The maximum stress change among each cell in red and black line region is calculated.

$$\Delta \sigma_{zz}'(t) = -\Delta P(t) \tag{10}$$

These stress changes are added to the *in-situ* stress to determine time dependent variation in the stress and the resulting stress tensor can be used to calculate the Coulomb stress change (van Wees et al., 2019) or Shear Capacity Utilization (Buijze et al., 2017), which for a fault plane is defined as:

$$SCU = \frac{\sigma_s}{C + \mu \sigma'_n},\tag{11}$$

where σ_s is the shear stress, σ'_n is the effective normal stress, C is cohesion and μ is the friction coefficient (corresponding to the tangent of the friction angle j).

The shear stress and effective normal stress on the fault plane are calculated from the normal of the fault plane $\bf n$ and the effective stress tensor $\bf \sigma'$ with a few simplified assumptions on the orientation of the stress components (Worum et al., 2004). For *in-situ* stress conditions and fault frictional parameters, we adopted parameters in agreement with previous geomechanical reservoir studies in the Netherlands (Van Wees et al., 2014; Buijze et al., 2017, 2021):

- The lithostatic stress gradient g_L (vertical total stress gradient) is assumed to be 24 MPa/km and hydrostatic pressure gradient (based on brine) to be 10.6 MPa/km to derive the initial vertical stress: $\sigma_{zz}^{'}(t=0)=(g_L)~z-P$
- The minimum and maximum effective horizontal stresses (σ'_h) and σ'_H are determined by the horizontal to vertical effective stress ratios k_0 (chosen 0.6) and k_1 (chosen 0.9) with $\sigma'_h(t=0) = k_0 \sigma'_{zz}$ and $\sigma'_H(t=0) = k_1 \sigma'_{zz}$
- ullet The orientation of σ_h is assumed to be perpendicular to the average map trends of the faults
- \bullet For the faults, the cohesion has been set to 2 MPa, and friction angle to 30°

We note that the uniaxial approach for estimating stress changes and adopting uniform elastic study is a strongly simplified approach. A more sophisticated geomechanics simulator would be needed to assess more complex stress interactions such as stress arching and the effect of local variations in mechanical properties. On the other hand, for matrix permeability dominated geothermal reservoirs, stress arching effects appear to be limited (Buijze et al., 2019) and uniaxial stress assumptions are capable to capture well first-order stress effects (Kivi et al., 2022; Marelis et al., 2023). Nevertheless, it should be noted that, in this study, the adopted uniaxial approximation serves primarily to showcase the relevance and capability of including fault stability considerations in the optimization procedure.

In this case, the output constraint function can be expressed mathematically as:

$$\mathbf{g}_{SCU}(\mathbf{u}) = \max_{1 \le \mathbf{v} \le N_t} SCU_{N_t}^{\mathbf{x}}(\mathbf{u}) \le 1, \tag{12}$$

where $SCU_{N_t}^x$ is the Shear-Capacity Utilization indicator computed as in eq. ${}_{,}SCU = \frac{\sigma_s}{C + \mu \sigma_n}$ (11 at the x grid cell adjacent to the fault at the last simulation time-step, N_b is the number of grid cells adjacent to the fault. Once again, this is repeated for each of the two faults separately in Upper and Lower formations, resulting in a total of 4 output constraint functions.

5. Optimization experiments

5.1. Unconstrained optimization

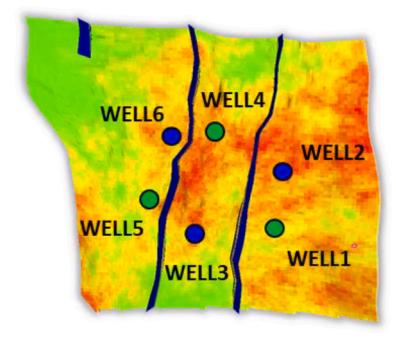
In this set of experiments, both well type and production rate optimization experiments are performed and compared to the base case corresponding to the initial well type configuration depicted in Fig. 6 (left), which serves as the starting point for the first optimization experiment, i.e. well type optimization. In the initial strategy the target well production was split evenly between the Upper and Lower formations.

5.1.1. Well type optimization

In the first experiment (Experiment 1) types of the wells were optimized. Each well can be either an injector or a producer while the locations and the trajectories of the wells are fixed. As previously mentioned in Section 4.4, the field water injection rate has been assigned dynamically to ensure reinjection of the produced volumes with a combination of group control keywords by the reservoir flow simulator. The individual well production and injection rate targets for each formation were also controlled.

An optimized well type configuration was obtained by running EVEReST with the ensemble of 40 model realizations. In the obtained optimal strategy two of the wells switched types compared to initial guess. Producer WELL1 became an injector while its neighbor (injector WELL3) became a producer. This resulted in a non-trivial well type configuration, depicted in Fig. 6. By switching the types of those two wells, the average NPV of the ensemble of models was increased by 8 million ϵ . A significant inflection of the cashflow curve is observed after a period of 15 years, which corresponds to the end of the period subject to subsidized heat price, see Fig. 7.

The temperature profiles in the wells that remained of the same type (i.e., WELL4 and WELL5) did not change much. The highest impact on NPV is associated with setting WELL3 as producer instead of WELL1. The new producer has a more favorable temperature profile in time: it



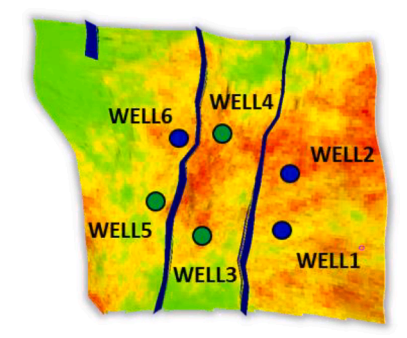


Fig. 6. Initial well types on the left and optimal well types on the right; blue color indicates injector and green indicates producer.

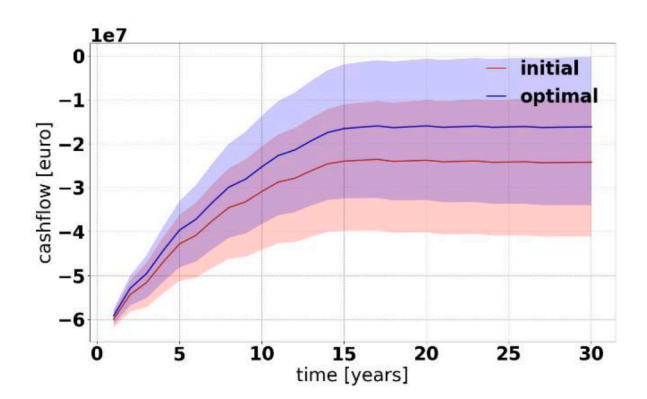


Fig. 7. Comparison of cashflow over time for initial and optimal strategy and for all realizations in Experiment 1. The solid lines indicate mean values while the filled area corresponds to minimum and maximum.

maintains higher production temperatures over a longer period of time (Fig. 8). We also noticed that the production temperature at the start is higher in the new producer, which can be attributed to the placement of this well in a deeper area of the reservoir accessing higher temperatures. As a matter of fact, we observe that the three deepest wells are set as

producers in the optimal well type configuration (Fig. 9).

In Experiment 2, well types were optimized by allowing production from Upper and Lower formations individually. The target flow rates for producers were split evenly between the formations. The flow rate in each well for Upper and Lower formations was determined by the flow simulator. This type of modelling provided us insight into the behavior of the system for particular formations.

The optimal solution found was the same as in the first experiment: WELL1 became a producer, and WELL3 turned into an injector. The average NPV improved by 6.6 million ϵ (Fig. 10). A more detailed analysis of the results shows that the cold-water breakthrough in the Upper formation occurs much earlier than in Lower formation as a result of the geological properties of formations (i.e., higher permeability in Upper formation) and the shorter distance between the wells in top formation due to the well drilling trajectory (Fig. 11). These temperature profiles indicate that optimizing well rates separately per formation could benefit from the possibility of increasing the production rate targets of the Lower formation. This also leads to questions about the possibility of reaching the techno-economic target for the studied field with heat production from Lower formation only. These two points are addressed in the optimization experiments to be presented next.

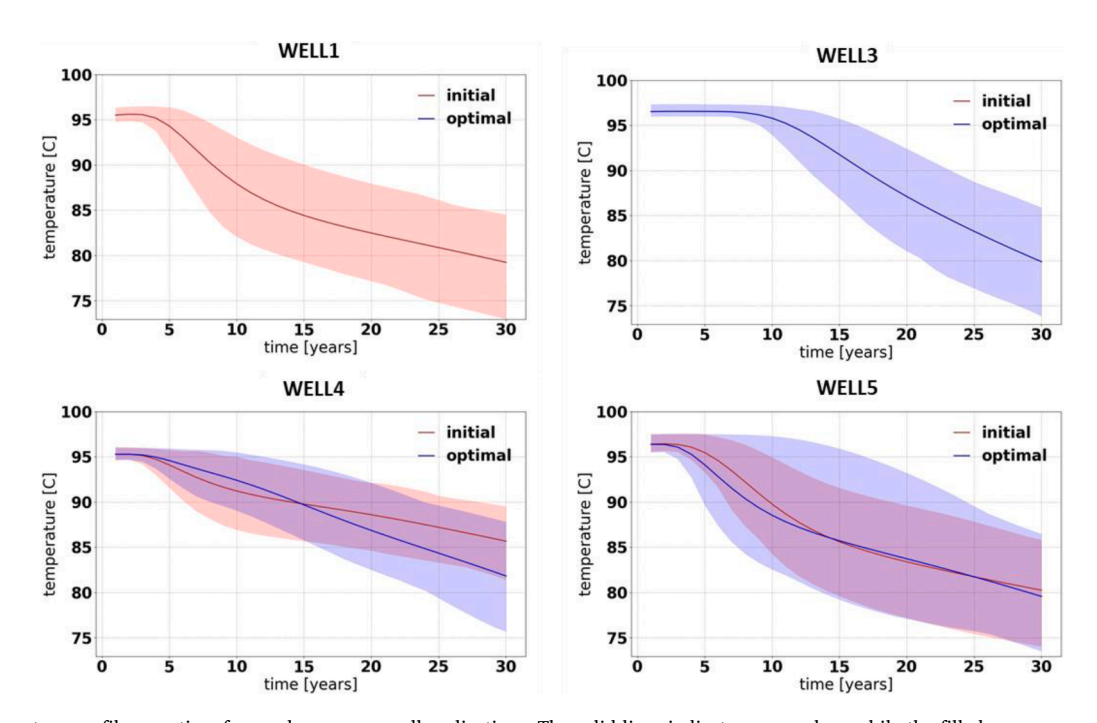


Fig. 8. The temperature profile over time for producers across all realizations. The solid lines indicate mean values while the filled area corresponds to minimum and maximum.

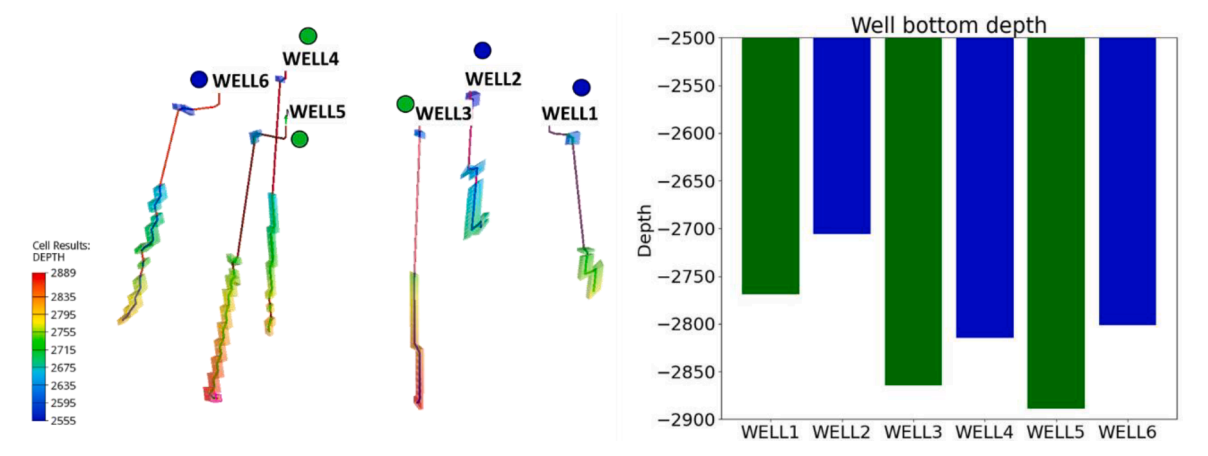


Fig. 9. Well trajectories and grid cell depth for all wells are shown on the left, vertical scale 5:1. Bottom depth (negative) for each well is shown on the right. Green color corresponds to producers and blue to injectors.

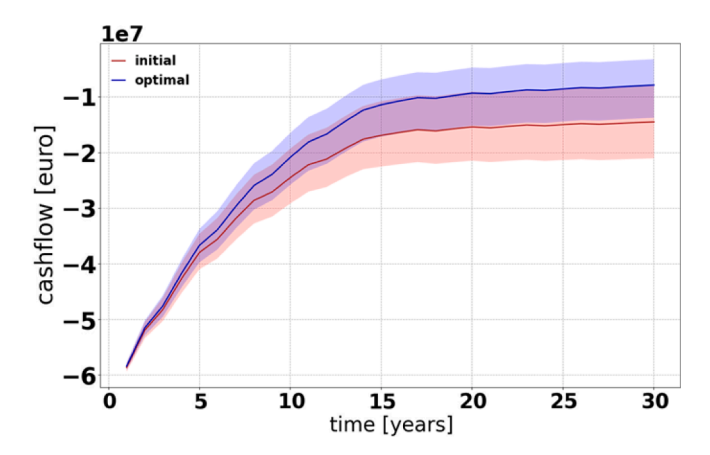


Fig. 10. Comparison of cashflow over time for initial and optimal strategy and for all realizations in Experiment 2. The solid blue lines indicate mean values while the filled area corresponds to minimum and maximum.

5.1.2. Well rate optimization

As a next step (Experiment 3), we fix the optimal well types (from Experiment 2) and focus on the optimization of well production rates. Rates are no longer evenly split between the top and bottom formations, but instead we seek their values through optimization. The total well rate targets (from Upper and Lower formations rates combined together) remain at 350 \mbox{m}^3/\mbox{h} . All rates are kept constant in time.

The results obtained in this optimization experiment show that the impact of varying the rate targets across formations is much larger than changing well types in the studied case. The average NPV increased by 17 million ϵ , see Fig. 12. Despite the increased uncertainty in NPV (i.e., large blue area in Fig. 12), the vast majority of the models improved with respect to the initial case (red area in Fig. 12).

In the optimal case, the NPV is improved due to a significant increase of production rate targets in the Lower formation accompanied by a reduction of production in the Upper formation (Fig. 13). More heat can then be extracted from the Lower formation. In addition, decreasing flow rates in the wells in top formation delays the cold-water breakthrough in that formation, as it can be seen in Fig. 14. The results show that, despite benefiting from the increased rates in the Lower formation, the production from the Upper formation still contributes positively to improve the field development project economics. This is due to the fact that the total target rate for any of the wells could not be reached with the influx from the Lower formation alone, see Fig. 13. In fact, we verified that, when shutting down the production from the Upper formation, the NPV is expected to decrease by 8 million ϵ .

5.2. Constrained optimization

5.2.1. Well rate optimization

In this section, we consider optimization with constraints on stress changes in time at the fault locations. The stress change is computed as Shear Capacity Utilization (see Section 4.5.3). The SCU indicator incorporates both pressure and temperature effects on the stress change. In the studied case, SCU is mostly correlated to the temperature changes taking place in the reservoir. Because in these experiments concern fault stability aspects, a refined analysis of the expected fault transmissibility was performed, and the fault transmissibility in the Lower formation has been reduced to values between 0 and 30 % with average of 20 % due to clay smearing. The fault transmissibility in Upper formation remained the same as previously, i.e., between 50 % and 100 %.

Prior to this analysis based on the SCU indicator, we have considered constraints related to the pressure difference across faults, which indicated that a line drive configuration with one doublet per reservoir compartment aligned parallel to fault orientation (Fig. 15) would the most favorable to preserve the stability of faults (in terms of pressure differences). For the sake of brevity, those results are not reported in this paper.

We repeat the well rate optimization experiment with SCU constraints for the identified line drive well type configuration (Experiment 4). The constraint target is for the SCU indicator to remain below 1.0.

As shown in Figs. 16 and 17, the SCU constraint is not satisfied for the majority of the models in the case with initial rates. It is particularly recognizable for the faults in Upper formation, where the SCU is higher than 1 for all the models. In the optimal strategy the SCU constraints are significantly lower. The consequence of keeping the SCU constraint at reduced levels is to significantly lower the injection/production rates (see Fig. 18), which significantly impacts the economics of the project, pointing to the need of reconsidering well drilling locations.

5.2.2. Well location optimization

The previous experiment has pointed to the importance of the location of the injection wells for fault stability purposes. Therefore, we optimized well rate targets in combination with the locations (i.e., x and y spatial coordinates) of 2 injectors in a scenario with 4 wells only (Experiment 5), once again including SCU constraints. The two wells in the middle compartment between the two faults have been removed since there was no viable injection strategy due to proximity to the faults (i.e., even with low injection rates, the cold water front originating from the injector in the middle compartment would reach the faults, causing the SCU constraints to be violated). Note that the costs associated with the drilling of those wells have been removed as well. The 2 remaining producers were kept fixed at their initial locations. We started this

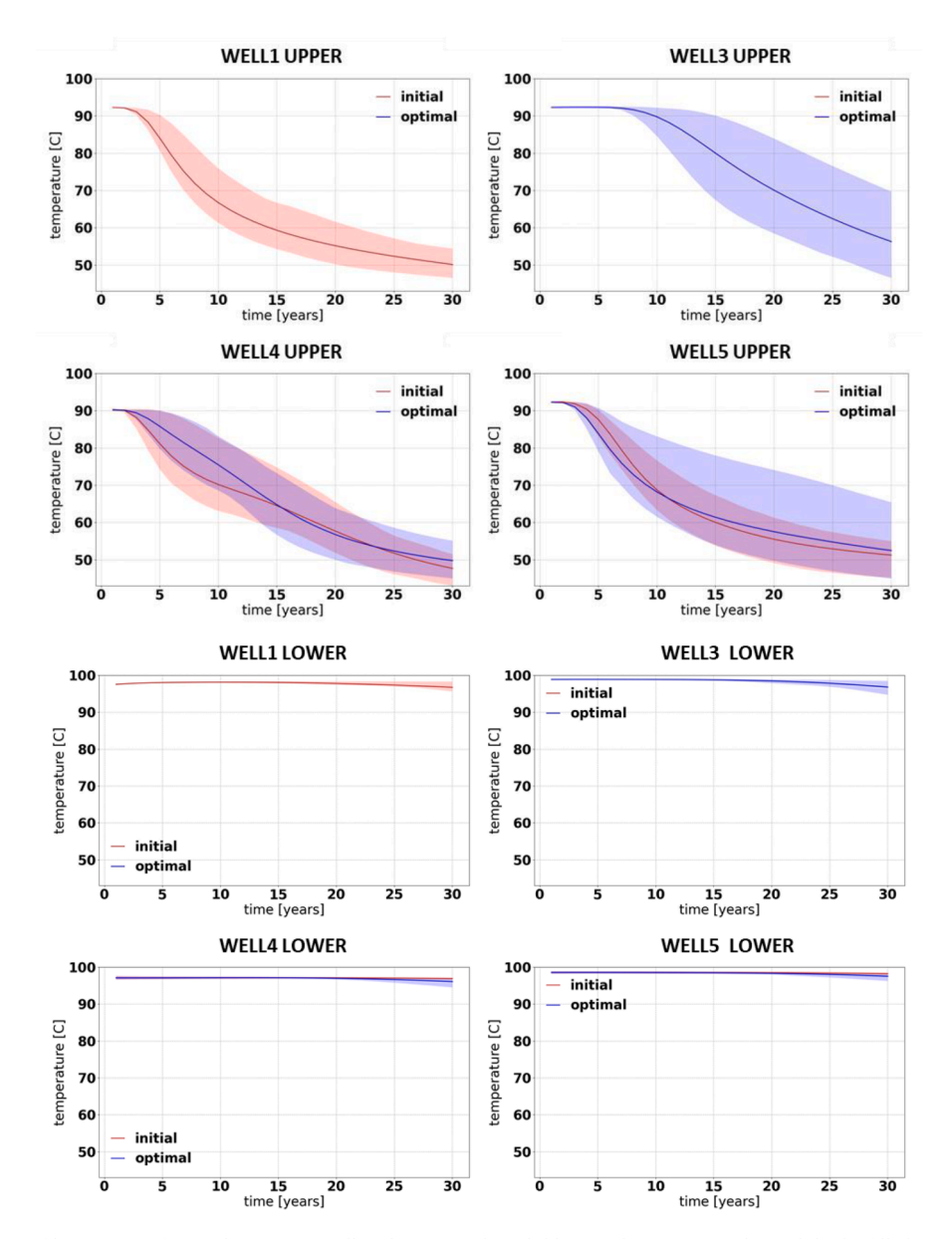


Fig. 11. The temperature profile over time for producers across all realizations. The solid lines indicate mean values while the filled area corresponds to minimum and maximum for all realizations. Top 4 figures represent temperature in the well in Upper formation Member and bottom 4 figures show well temperature in Lower formation Member.

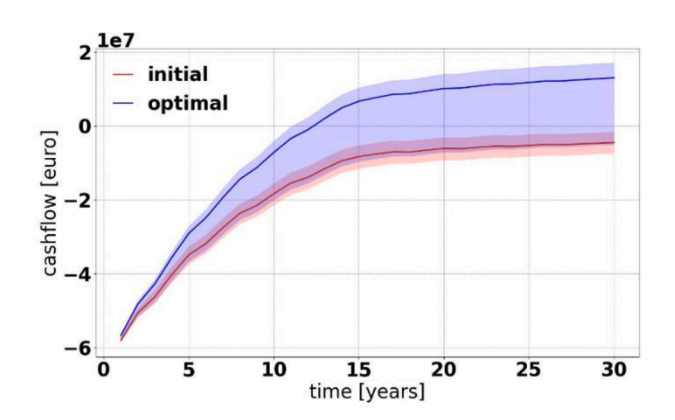


Fig. 12. Comparison of cashflow over time for initial and optimal strategy and for all realizations in Experiment 3. The solid blue lines indicate mean values while the filled area corresponds to minimum and maximum.

optimization with the initial well locations for the two concerned injectors. For simplicity, the well trajectories were assumed vertical, following a particular case of the more general computational workflow proposed by Barros et al. (2020) for optimization of more complex well trajectories. Every time the wells are relocated during the optimization process, the appropriate well connection transmissibility factors are recomputed and provided to the reservoir simulation.

In the optimal strategy, the injectors were placed far away from the faults (Fig. 19). Injector WELL6 was moved further than injector WELL2. Moving injector WELL2 any further would result in the well positioning outside of the reservoir, particularly missing the Lower formation. Losing an injector would lower project revenues because lower injection leads to lower production rates in a closed system. The results highlight the importance of optimizing well trajectories in combination with well locations when fault stability is of concern.

Once the injectors are further away from the faults, higher injection rates can be achieved (Fig. 20) without breaking the SCU constraints (Fig. 22). Optimizing well rate targets and locations of two injectors in a

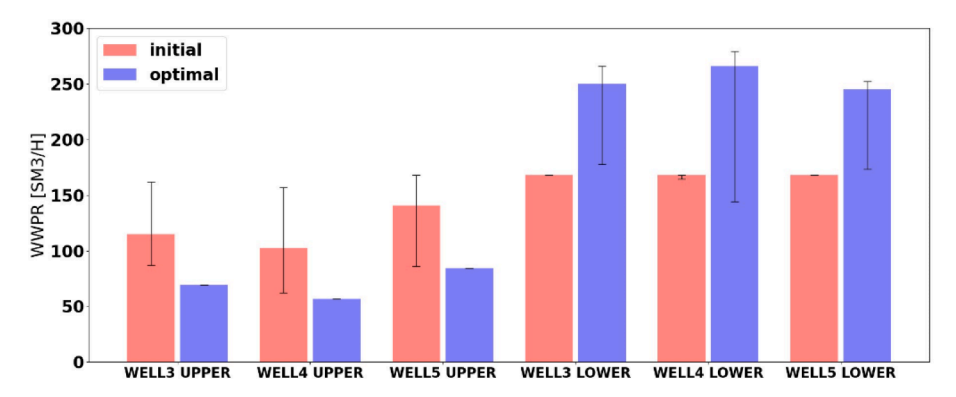


Fig. 13. Comparison of well production rate targets in producers between initial and optimal strategies. The top of the bar corresponds to the average and the whiskers correspond to the minimum and maximum across the realizations.

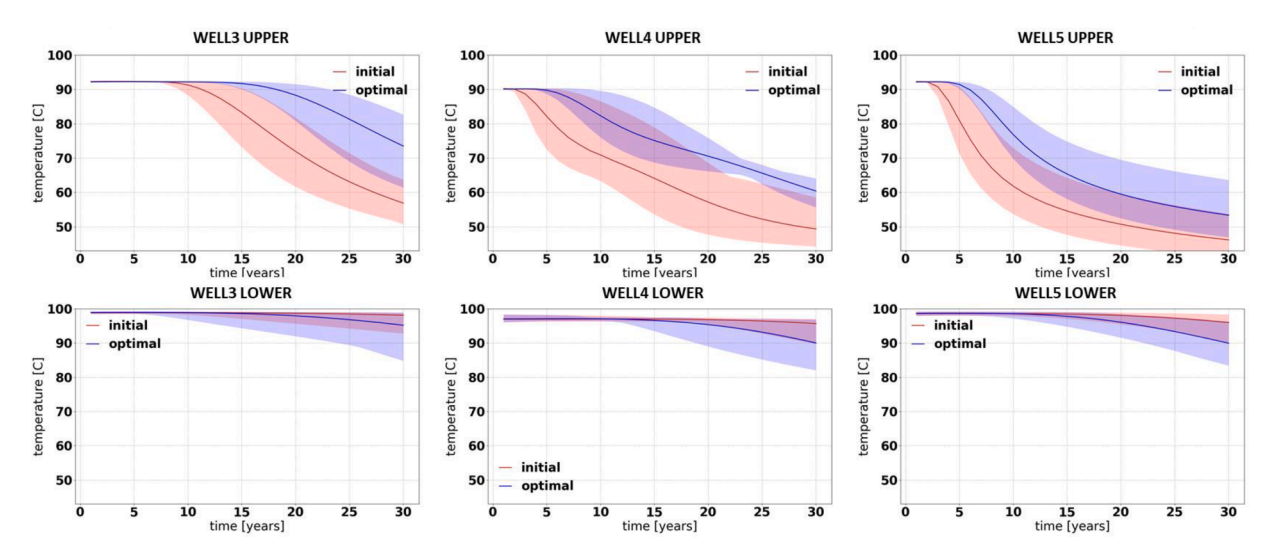


Fig. 14. The temperature profile over time for producers across all realizations. The solid lines indicate mean values. The filled area corresponds to minimum and maximum.

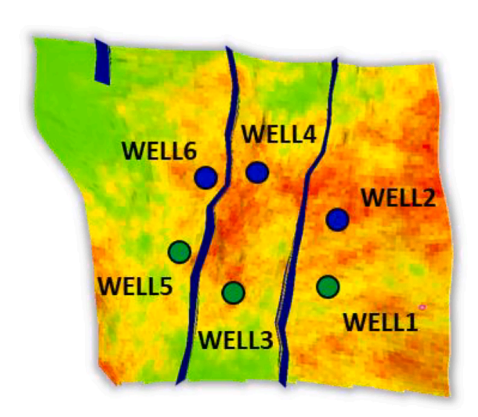


Fig. 15. Line drive well type configuration parallel to fault orientation.

4-well scenario resulted in the NPV comparable to initial strategy with 6 wells (see cashflow for current experiment in Fig. 21). The CAPEX is reduced due to lower drilling cost associated with fewer wells. Even though optimization of well types and well rates for the 6-well scenario without constraints resulted in increase of 17 million ϵ (see Experiment 3), this optimal strategy was obtained without considering risk associated with fault stability. In fact, for the initial well placement, the optimal well rates in the constrained scenario were reduced

significantly, making project economically unattractive. This shows that well placement is a very important aspect when considering fault stability risk and that optimization can help find the optimal combination of well rate and well locations.

5.3. Computational costs

Implementing a manual optimization methodology becomes impractical when dealing with a large number of decision variables. In this work, we considered the selection of various well production rate values and configurations for six wells, assessed across 40 model realizations while respecting fault stability constraints, which renders the optimization problem even more complex and inviable to be solved with a manual approach. The most time-intensive step in the computerassisted workflow was the numerical flow simulation of the subsurface model. The optimization experiments in this study converged between 12 and 31 iterations, where each iteration involved 40 model simulations to assess the current best strategy for each geological model, with an additional 40 to construct the gradient. All simulations are independent, and the computational cost of assembling the gradient is negligible compared to numerical simulations. Consequently, with access to a high-performance computing (HPC) cluster with capacity to accommodate the entire batch of 80 (40 + 40) simulations in each iteration, the time cost of the longest experiment was approximately the time equivalent to 31 numerical model simulations run serially. All numerical model simulations were performed on a HPC cluster, with a

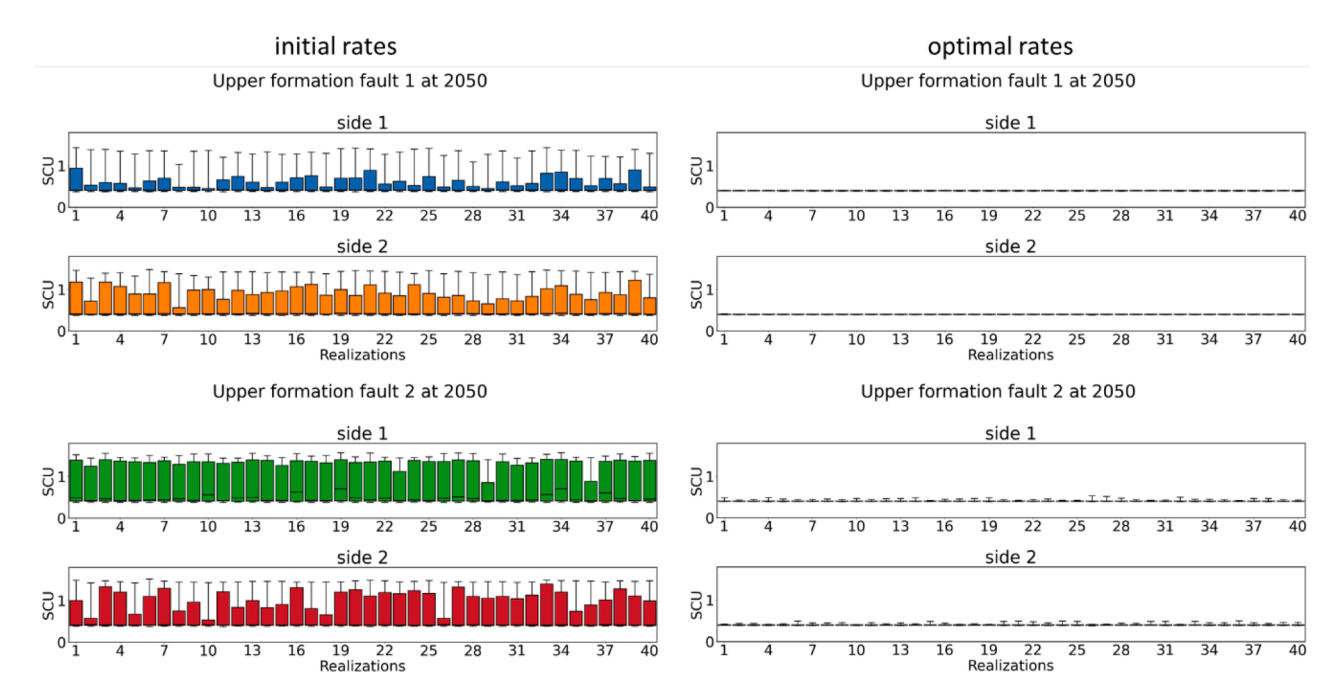


Fig. 16. SCU constraint for both sides of both Upper formation faults for all models. Results for initial well rates (on the left) and optimal rates (on the right). The box plots represent statistics for all the cells connecting the fault. The solid line represents the average, the box represents the 25th and 75th quantile and the whiskers represent minimum and maximum values.

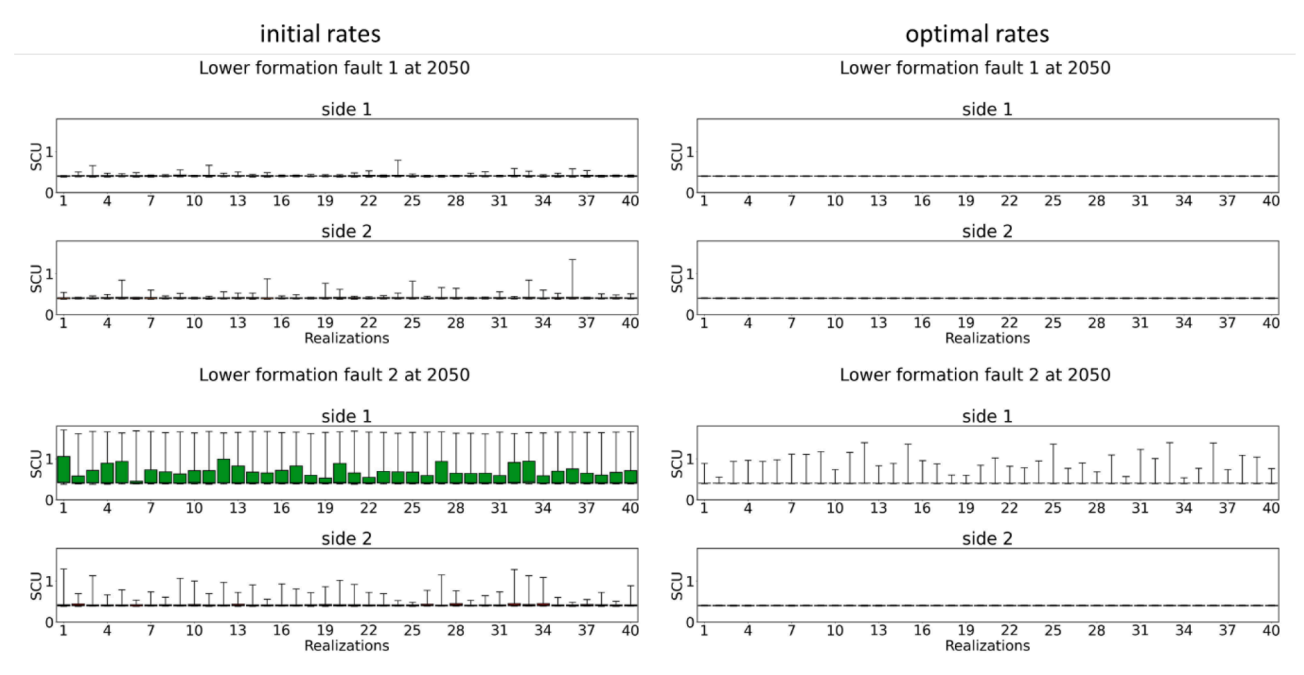


Fig. 17. SCU constraint for both sides of both Lower formation faults for all models. Results for initial well rates (on the left) and optimal rates (on the right). The box plots represent statistics for all the cells connecting the fault. The solid line represents the average, the box represents the 25th and 75th quantile and the whiskers represent minimum and maximum values.

single model simulation taking between 1h and 4h. As an indication, the longest experiment out of the 7 performed took approximately 6 days of total simulation time. A similar effort based on a laborious manual approach would likely have taken significantly more time and attention of engineers, whereas, with the computer-assisted approach, the engineer has time to dedicate to other activities while the simulations are run in an automated manner.

6. Conclusions

The goal of this study was to demonstrate the use of optimization to support geothermal practitioners in the search for improved field development concepts applicable to a real-life case study, representative of typical reservoir formations for geothermal plays in the Netherlands. An ensemble of dynamic numerical models was created to represent the subsurface uncertainty and is suitable for optimization under geological uncertainty. We have made realistic albeit generic assumptions on the economics of the project. State-of-the-art optimization technology based

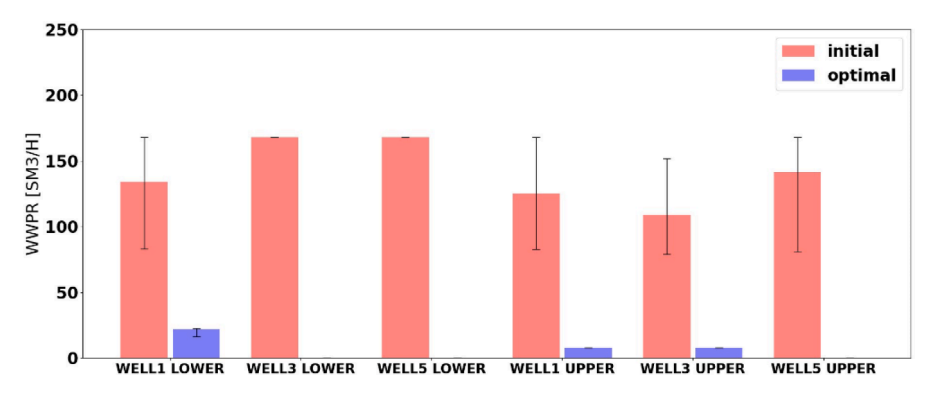


Fig. 18. Initial and optimal rates for optimization with SCU constraints for the 6-well scenario. The top of the bar corresponds to the average and the whiskers correspond to the minimum and maximum across the realizations.

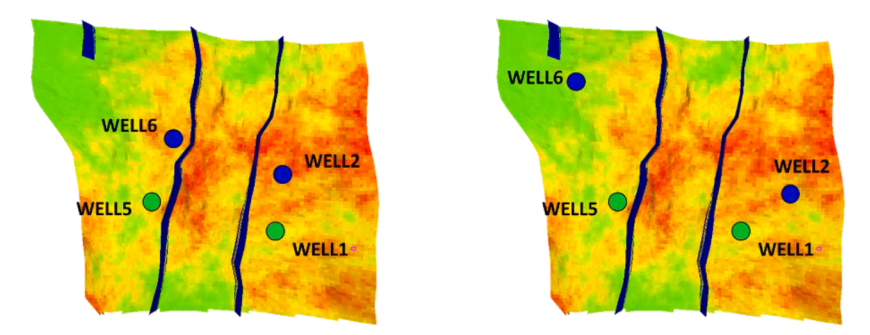


Fig. 19. Initial and optimal well locations in Experiment 5.

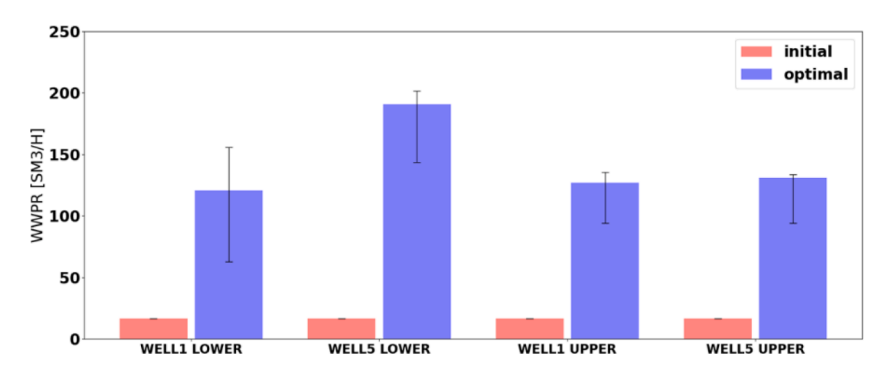


Fig. 20. Initial and optimal rates for optimization with SCU constraints for a 4-wells-scenario. The top of the bar corresponds to the average and the whiskers correspond to the minimum and maximum across the realizations.

on modern stochastic gradient-based methods was employed to enable robust optimization over an ensemble of model realizations in a computationally efficient manner. Well type selection, production flow rates and well locations were optimized for a case study with stacked reservoir layers. Significant improvements in terms of the project cumulative discounted cashflow (+17 million $\mathfrak E$) were achieved using optimization. In addition, the effect of field development on nearby fault stability has been studied, including the impact of imposing fault stability constraints in the optimization procedure.

In terms of scientific contributions, this work highlights the integration of advanced multi-physics computational workflows, demonstrating their potential to refine the conventional best-practices in field development planning within the geothermal sector, namely:

 Robust computer-assisted optimization based on a set of model realizations to capture the inherent geological uncertainties throughout the optimization process, as opposed to relying on a single base case model in conventional engineering-based optimization.

- Optimization of different field development decisions, i.e. well types
 / locations and production rate targets.
- Integrating numerical flow simulation with a simplified parametric geomechanical model to incorporate fault stability limits throughout the field development optimization exercise.
- Systematic design of a series of unconstrained and constrained optimization experiments to gain quantitative understanding of the impact of the various optimization variables and constraints.
- Quantification of uncertainties with respect to objective function and output constraint functions simultaneously to guide the robust optimization process.

Regarding current limitations of the presented approaches, we can identify the following points for potential future improvements:

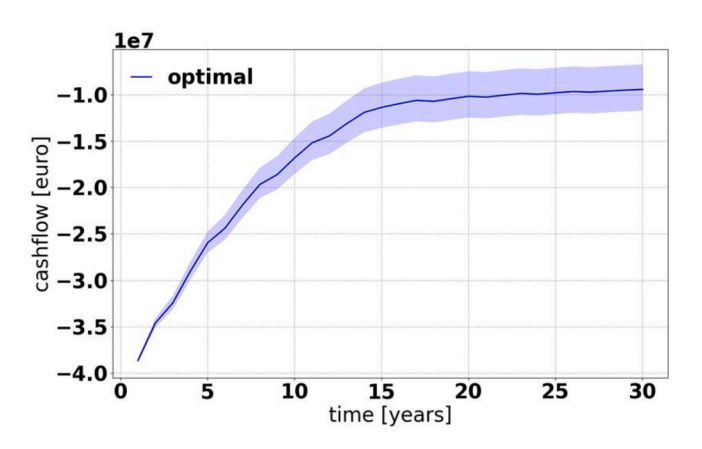


Fig. 21. Cashflow over time for optimal strategy and for all realizations in Experiment 5. The solid blue lines indicate mean values. The filled area corresponds to minimum and maximum.

- The fault stability aspect is limited to the SCU indicator based on simplified uniaxial stress assumptions. More sophisticated calculation approaches can be adopted by considering the entire stress tensor. Moreover, it is possible to extend the workflow and derive induced seismicity effects resulting from fault activation events, which could be used as additional constraints for the optimization process to ensure safe field development strategies.
- While several geological uncertainties have been accounted for, the location of the faults was assumed to be known in this study. Because the constraints imposed are strongly related to the reservoir state at the fault locations, considering different fault position scenarios could impact the results.
- Throughout all performed experiments, the surface drilling location
 was assumed to be fixed. Since we consider an economic objective
 function with strong dependence on well costs and their length,
 optimizing the drilling location could help further improve the
 economics of the project.
- Fault stability constraints have been imposed to be honored on average across the ensemble of 40 model realizations. A more conservative approach would be to impose constraints to worst-case scenario, to guarantee that all the 40 model realizations do not violate the fault stability limits.

Analysis of results from the several performed optimization

experiments have led to a series of key findings applicable beyond the case study considered:

- Optimization can help find case-specific optimal production strategy while taking into consideration the geological uncertainty and risk constraints.
- The first choice of field development configurations conceived by practitioners based on previous experiences might not always lead to the best performance.
- Some learnings from optimization confirm operational experience, e. g., placing injectors further away from the faults, placing producers deeper.
- Different behavior for individual model realizations (e.g., performance, adherence to constraints) underlines importance of accounting for uncertainty within optimization. Working with a single model may lead to accepting field development concepts that should actually be discarded.
- Computer-assisted optimization allows practitioners to vary many parameters simultaneously to obtain optimal outcome. A broad range of alternatives can be evaluated, which would otherwise never be considered.
- Computer-assisted optimization can reduce time and effort required (both manual and computational) by practitioners to find optimal strategies. This frees time for domain expertise to be used to understand the behavior of the reservoir and why optimized strategies improve performance.
- Analysis of optimization results in different contexts (considering different control types, constraints, geological settings, etc.) helps understanding which parameters significantly impact the system performance in terms of economics, safety, and sustainability.

Reflecting on the learnings more specific to the target case study, we can highlight the following:

- The combination of well depth and flow interaction affects the optimal well type configuration.
- For stacked reservoirs producing from individual geological formations at different rates can increase performance. In such cases, the best strategy depends on the flow properties of the formations.
- Fault stability risk related across the faults can be mitigated by choosing a line-drive strategy parallel to fault orientation and reducing production rates, leading however to significantly lower NPV.

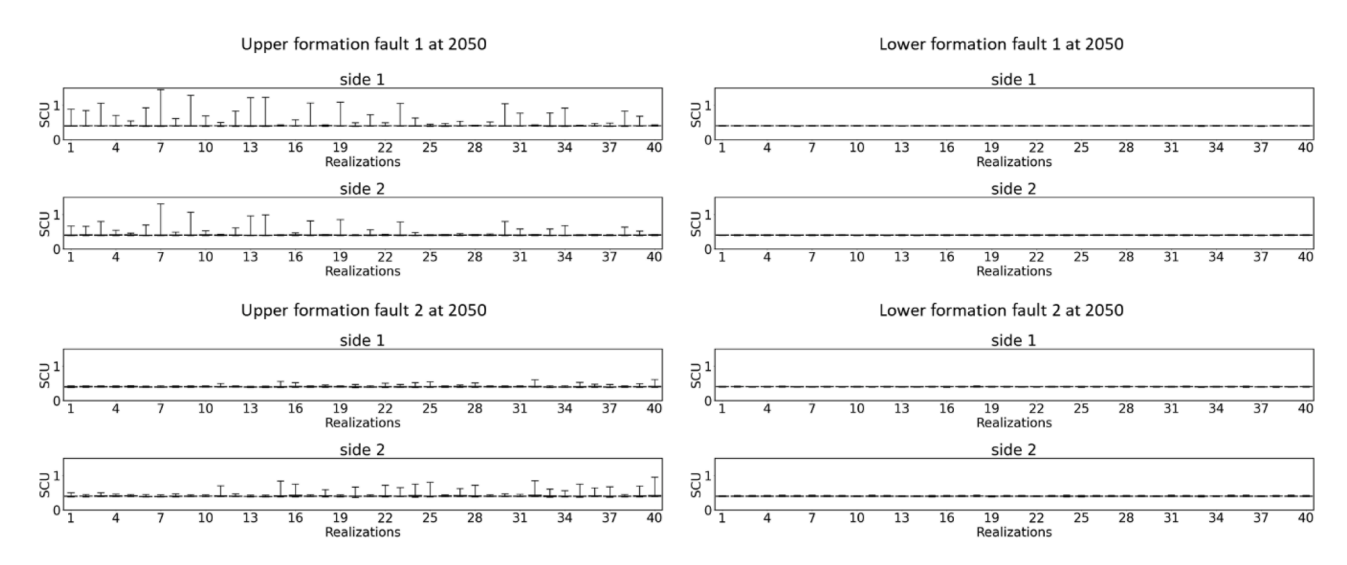


Fig. 22. SCU constraint for both sides of all the faults for all models. Results for optimal rates. The box plots represent statistics for all the cells connecting the fault. The solid line represents the average, the box represents the 25th and 75th quantile and the whiskers represent minimum and maximum values.

 The cold temperature front is important for stress changes at faults, which control their stability. Therefore, drilling the injection wells further away from the faults may help achieve higher production flow rates while keeping stress changes to acceptable levels.

CRediT authorship contribution statement

S.P. Szklarz: Writing – review & editing, Writing – original draft, Visualization, Validation, Software, Methodology, Investigation, Formal analysis, Conceptualization. **E.G.D. Barros:** Writing – review & editing, Writing – original draft, Supervision, Methodology, Formal analysis, Conceptualization. **N. Khoshnevis Gargar:** Writing – review & editing, Writing – original draft, Validation, Methodology, Investigation, Formal analysis. **S.H.J. Peeters:** Writing – review & editing, Writing – original draft, Methodology, Investigation. **J.D. van Wees:** Writing – review & editing, Supervision, Conceptualization. **V. van Pul-Verboom:** Project administration.

Declaration of competing interest

The authors declare the following financial interests/personal relationships which may be considered as potential competing interests:

TNO reports financial support was provided by Netherlands Enterprise Agency. If there are other authors, they declare that they have no known competing financial interests or personal relationships that could have appeared to influence the work reported in this paper.

Data availability

The data that has been used is confidential.

Acknowledgments

This project has been performed as part of the WarmingUP Program subsidized by the Netherlands Enterprise Agency (RVO) in the context of the Multi-Year Mission-Driven Innovation Programs (MMIP4: Sustainable heat and cold in the built environment) subsidy scheme, known at RVO under project number TEUE819001. We would also wish to thank the partners of this specific project in the program: EBN BV, ENGIE Energy Solutions BV, Gemeente Breda, Huisman Geo BV, HVC Warmte BV and Shell Geothermal BV (in alphabetical order).

References

- Akın, S., Kok, M.V., Uraz, I., 2010. Optimization of well placement geothermal reservoirs using artificial intelligence. Comput. Geosci. 36 (6), 776–785.
- Alberty, M. (1992). "Standard interpretation: part 4. wireline methods".
- Amoatey, P., Chen, M., Al-Maktoumi, A., Izady, A., Baawain, M.S., 2021. A review of geothermal energy status and potentials in Middle-East countries. Arab. J. Geosci. 14, 1–19.
- Anderson, A., Rezaie, B., 2019. Geothermal technology: trends and potential role in a sustainable future. Appl. Energy 248, 18–34.
- Andritsos, N., Dalabakis, P., Karydakis, G., Kolios, N., Fytikas, M., 2011. Characteristics of low-enthalpy geothermal applications in Greece. Renew. Energy 36 (4), 1298–1305.
- Arola, T., Eskola, L., Hellen, J., Korkka-Niemi, K., 2014. Mapping the low enthalpy geothermal potential of shallow quaternary aquifers in Finland. Geotherm. Energy 2, 1–20.
- Barros, E., Fonseca, R., De Moraes, R., 2019. Production optimisation under uncertainty with automated scenario reduction: a real-field case application. In: Proceedings of the SPE Reservoir Characterisation and Simulation Conference and Exhibition. OnePetro.
- Barros, E., Ruan, P., Ishmuratov, R., Hopman, J., Fonseca, R., 2020a. Hydraulic fracture stage design optimization of a dry gas field in the North Sea. In: Proceedings of the EAGE 2020 Annual Conference & Exhibition Online. European Association of Geoscientists & Engineers.
- Barros, E., Van Aken, B., Burgers, A., Slooff-Hoek, L., Fonseca, R., 2022. Multi-objective optimization of solar park design under climatic uncertainty. Sol. Energy 231, 958–969.

Barros, E.G., Chitu, A., Leeuwenburgh, O., 2020b. Ensemble-based well trajectory and drilling schedule optimization—Application to the Olympus benchmark model. Comput. Geosci. 24 (6), 2095–2109.

- Birkle, P., Bundschuh, J., 2007. High and low enthalpy geothermal resources and potential. In: Bundschuh, J., Alvarado, G.E. (Eds.), Central America: Geology, resources and hazards, 2. Taylor & Francis, Leiden, pp. 707–777.
- Blank, L., Rioseco, E.M., Caiazzo, A., Wilbrandt, U., 2021. Modeling, simulation, and optimization of geothermal energy production from hot sedimentary aquifers. Comput. Geosci. 25 (1), 67–104.
- Buijze, L., Fokker, P., Wassing, B., 2021. Quantification of induced seismicity potential of geothermal operations: analytical and numerical model approaches. Sci. Rep. TNO, Utrecht (Published in the framework of WarmingUp Theme 4B).
- Buijze, L., van Bijsterveldt, L., Cremer, H., Jaarsma, B., Paap, B., Veldkamp, H., Wassing, B., van Wees, J., van Yperen, G., Ter Heege, J., 2019. Induced seismicity in geothermal systems: occurrences worldwide and implications for the Netherlands. In: Proceedings of the European Geothermal Congress.
- Buijze, L., van den Bogert, P.A., Wassing, B.B., Orlic, B., ten Veen, J., 2017. Fault reactivation mechanisms and dynamic rupture modelling of depletion-induced seismic events in a Rotliegend gas reservoir. Neth. J. Geosci. 96 (5), s131–s148.
- Chen, Y., Oliver, D.S., Zhang, D., 2009. Efficient ensemble-based closed-loop production optimization. SPE J. 14 (4), 634–645.
- Chen, M., Tompson, A.F., Mellors, R.J., Abdalla, O., 2015. An efficient optimization of well placement and control for a geothermal prospect under geological uncertainty. Appl. Energy 137, 352–363.
- De Giorgio, G., Chieco, M., Limoni, P.P., Zuffianò, L.E., Dragone, V., Romanazzi, A., Pagliarulo, R., Musicco, G., Polemio, M., 2020. Improving regulation and the role of natural risk knowledge to promote sustainable low enthalpy geothermal energy utilization. Water 12 (10), 2925 (Basel).
- Den Hartog Jager, D., 1996. Fluviomarine sequences in the lower cretaceous of the West Netherlands Basin: correlation and seismic expression. Geology of Gas and Oil Under the Netherlands. Springer, pp. 229–241.
- Dhansay, T., de Wit, M., Patt, A., 2014. An evaluation for harnessing low-enthalpy geothermal energy in the Limpopo Province, South Africa. S. Afr. J. Sci. 110 (3–4), 01–10.
- Donselaar, M.E., Groenenberg, R.M., Gilding, D.T., 2015. Reservoir geology and geothermal potential of the Delft Sandstone Member in the West Netherlands Basin. In: Proceedings of the World Geothermal Congress.
- Fjaer, E., Holt, R.M., Horsrud, P., Raaen, A.M., 2008. Petroleum Related Rock Mechanics. Elsevier.
- Fonseca, R.R.M., Chen, B., Jansen, J.D., Reynolds, A., 2017. A stochastic simplex approximate gradient (StoSAG) for optimization under uncertainty. Int. J. Numer. Methods Eng. 109 (13), 1756–1776.
- Fridleifsson, I.B., Bertani, R., Huenges, E., Lund, J.W., Ragnarsson, A., Rybach, L., 2008. The possible role and contribution of geothermal energy to the mitigation of climate change. In: Proceedings of the IPCC Scoping Meeting on Renewable Energy Sources. Luebeck. Germany. Citeseer.
- Hanea, R.G., Bjorlykke, O.P., Hashmi, Y., Feng, T., Fonseca, R.M., 2019. Robust multiobjective field development optimization for the mariner asset. In: Proceedings of the SPE Reservoir Simulation Conference. Texas, USA. OnePetro.
- Kahrobaei, S., Fonseca, R., Willems, C., Wilschut, F., Van Wees, J., 2019. Regional scale geothermal field development optimization under geological uncertainties. In: Proceedings of the European Geothermal Congress, pp. 11–14.
- Kim, J., Lee, Y., Yoon, W.S., Jeon, J.S., Koo, M.-H., Keehm, Y., 2010. Numerical modeling of aquifer thermal energy storage system. Energy 35 (12), 4955–4965.
- Kivi, I.R., Pujades, E., Rutqvist, J., Vilarrasa, V., 2022. Cooling-induced reactivation of distant faults during long-term geothermal energy production in hot sedimentary aquifers. Sci. Rep. 12 (1), 2065.
- Marelis, A., van Wees, J.-D., and Beekman, F. (2023). A sensitivity analysis of stress changes related to geothermal direct heat production in clastic reservoirs and potential for fault reactivation and seismicity. Paper presented at EGU General Assembly 2023, Vienna, Austria, 24-28 April. doi:10.5194/egusphere-egu23-14219.
- Martín-Gamboa, M., Iribarren, D., Dufour, J., 2015. On the environmental suitability of high-and low-enthalpy geothermal systems. Geothermics 53, 27–37.
- Meza, J.C., Oliva, R.A., Hough, P., Williams, P., 2007. OPT++ An object-oriented toolkit for nonlinear optimization. ACM Trans. Math. Softw. TOMS 33 (2), 12-es.
- Mijnlieff, H., Van Wees, J.D. (2009). "Rapportage ruimtelijke ordening geothermie." TNO report.
- Morton-Thompson, D., Woods, A.M., 1992. Development Geology Reference Manual. AAPG Methods in Exploration 10. doi:10.1306/Mth10573.
- Pluymaekers, M.P.D., Doornenbal, J.C., Middelburg, H. (2017). VELMOD-3.1, TNO 2017 R11014 with erratum. 67. https://www.nlog.nl/sites/default/files/2018-11/060.2 6839%20R11014%20with%20erratum%20page%2067%20Doornenbal-final.sec_. pdf.
- Rasmussen, A.F., Sandve, T.H., Bao, K., Lauser, A., Hove, J., Skaflestad, B., Klöfkorn, R., Blatt, M., Rustad, A.B., Sævareid, O., 2021. The open porous media flow reservoir simulator. Comput. Math. Appl. 81, 159–185.
- Rubio-Maya, C., Díaz, V.A., Martínez, E.P., Belman-Flores, J.M., 2015. Cascade utilization of low and medium enthalpy geothermal resources— A review. Renew. Sustain. Energy Rev. 52, 689–716.
- Schoof, F., van der Hout, M., van Zanten, J., van Hoogstraten, J., 2018. Master Plan Geothermal Energy in the Netherlands. Stichting Platform Geothermie, Delft, The Netherlands.
- Seo, S.N., 2017. Beyond the Paris agreement: climate change policy negotiations and future directions. Reg. Sci. Policy Pract. 9 (2), 121–140.
- Soltani, M., Moradi Kashkooli, F., Dehghani-Sanij, A., Nokhosteen, A., Ahmadi-Joughi, A., Gharali, K., Mahbaz, S., Dusseault, M., 2019. A comprehensive review of

- geothermal energy evolution and development. Int. J. Green Energy 16 (13), 971, 1000
- Swamy, S.K., Szklarz, S., Fonseca, R., Bulder, B., 2020. Combined wind turbine design and wind farm layout optimisation under wind resource uncertainty. J. Phys. Conf. Ser. 1618, 042030.
- Van Adrichem Boogaert, H.A., Kouwe, W.F.P., 1993. Stratigraphic nomenclature of the Netherlands, revision and update by RGD and NOGEPA. Section A, General. Mededelingen Rijks Geologische Dienst 50, 1–40.
- van Wees, J.D., Kronimus, A., van Putten, M., Pluymaekers, M.P.D., Mijnlieff, H., van Hooff, P., Obdam, A., Kramers, L., 2012. Geothermal aquifer performance assessment for direct heat production Methodology and application to Rotliegend aquifers. Netherlands Journal of Geosciences 91 (4), 651–665.
- van Wees, J.D., Veldkamp, H., Brunner, L., Vrijlandt, M., de Jong, S., Heijnen, N., van Langen, C., Peijster, J., 2020. Accelerating geothermal development with a playbased portfolio approach. Neth. J. Geosci. 99, e5.
- van Wees, J.-D., Pluymaekers, M., Osinga, S., Fokker, P., Van Thienen-Visser, K., Orlic, B., Wassing, B., Hegen, D., Candela, T., 2019. 3-D mechanical analysis of complex reservoirs: a novel mesh-free approach. Geophys. J. Int. 219 (2), 1118–1130.
- Van Wees, J., Buijze, L., Van Thienen-Visser, K., Nepveu, M., Wassing, B., Orlic, B., Fokker, P., 2014. Geomechanics response and induced seismicity during gas field depletion in the Netherlands. Geothermics 52, 206–219.
- Vanderplaats, G.N., 1984. An efficient feasible directions algorithm for design synthesis. AIAA J. 22 (11), 1633–1640.
- Vrijlandt, M., Struijk, E.L.M., Brunner, L.H., Veldkamp, J.G., Witmans, N., Maljers, D., Van Wees, J., 2019. ThermoGIS update: a renewed view on geothermal potential in the Netherlands. In: proc: European Geothermal Congress, 11-14 June. The Hague, the Netherlands.

- Wachowicz-Pyzik, A., Sowiżdżał, A., Pająk, L., Ziółkowski, P., Badur, J., 2020.
 Assessment of the effective variants leading to higher efficiency for the geothermal doublet, using numerical analysis-case study from Poland (Szczecin Trough).
 Energies 13 (9), 2174 (Basel).
- Willems, C., Goense, T., Nick, H.M., Bruhn, D., 2016. The relation between well spacing and net present value in fluvial hot sedimentary aquifer geothermal doublets; a West Netherlands Basin case study. In: Proceedings of the 41st Workshop on Geothermal Aquifer Engineering Stanford University.
- Willems, C., Nick, H., 2019. Towards optimisation of geothermal heat recovery: an example from the West Netherlands Basin. Appl. Energy 247, 582–593.
- Worum, G., van Wees, J.D., Bada, G., van Balen, R.T., Cloetingh, S., Pagnier, H., 2004. Slip tendency analysis as a tool to constrain fault reactivation: a numerical approach applied to three-dimensional fault models in the Roer Valley rift system (southeast Netherlands). J.Geophys. Res. Solid Earth 109 (B2).
- Yapparova, A., Matthäi, S., Driesner, T., 2014. Realistic simulation of an aquifer thermal energy storage: effects of injection temperature, well placement and groundwater flow. Energy 76, 1011–1018.
- Yielding, G., 2002. Shale gouge ratio—Calibration by geohistory. In: Norwegian Petroleum Society Special Publications, 11. Elsevier, pp. 1–15.
- Younger, P.L., 2015. Geothermal Energy: Delivering on the Global Potential, 8. MDPI, pp. 11737–11754.
- Zaal, C., Daniilidis, A., Vossepoel, F.C., 2021. Economic and fault stability analysis of geothermal field development in direct-use hydrothermal reservoirs. Geotherm. Energy 9 (1), 1–26.
- Zoback, M.D., 2010. Reservoir Geomechanics. Cambridge university press.Zoutendijk, G., 1960. Methods of Feasible Directions: a Study in Linear and Non-Linear Programming. Elsevier.